Phenotypic, genomic, and transcriptomic heterogeneity in a pancreatic cancer cell line

Gengqiang Xie[1], Olalekan H Usman[1], Sampath Kumar[1], Dhenu Patel[1], Megan Kavanaugh[1], Yue Julia Wang[1], and Jerome Irianto[1]*

[1]Department of Biomedical Sciences, College of Medicine, Florida State University, Tallahassee, FL 32306, USA

*Corresponding author: Jerome Irianto, Department of Biomedical Sciences, College of Medicine, Florida State University, 1115 West Call St, Tallahassee, FL 32306

Phone: 850-645-9438

E-mail: jerome.irianto@med.fsu.edu

Abstract

Intratumor phenotypic, genomic, and transcriptomic heterogeneity in pancreatic cancer have been reported by multiple studies; however, little is known about the heterogeneity's underlying mechanisms. One possible approach to studying this is to perform a mechanistic study using pancreatic ductal adenocarcinoma (PDAC) cancer cell lines that show such heterogeneity. Here, to evaluate the suitability of the MIA PaCa-2 cell line for studying heterogeneity, we further characterize the nature of MIA PaCa-2 cells' phenotypic, genomic, and transcriptomic heterogeneity. Four MIA PaCa-2 clones showed distinctive phenotypes, with differences in cellular morphology, proliferation rate, and migration potential. We also observed a degree of genomic variations between these clones in form of chromosome copy number alterations, suggesting the genomic heterogeneity of the population, and the intrinsic genomic instability of MIA PaCa-2 cells. Lastly, transcriptomic analysis of the clones also revealed gene expression profile differences between the clones, including uniquely regulated *ITGAV*, which dictates the morphology of MIA PaCa-2 clones. In conclusion, our study showed that MIA PaCa-2 is comprised of cells with distinctive phenotypes, heterogeneous genomes, and differential transcriptomic profiles, suggesting its suitability as a model to study the underlying mechanisms behind PDAC tumor phenotypic, genomic, and transcriptomic heterogeneity.

Key words: pancreatic cancer, genomic heterogeneity, MIA PaCa-2, ITGAV

Introduction

In most cancers, the transformed cells undergo cycles of genetic diversification, selection of adaptive clones, and clonal expansion, a process that mirrors Darwin's natural selection (*1*). Specific mutations provide a growth advantage to a subpopulation of cells, giving rise to the evolution of distinctive clones (*2*). The evolution process will then leads to a tumor comprised of cells with heterogeneous phenotypes, including response to therapy (*3*). This is certainly the case for pancreatic ductal adenocarcinoma (PDAC), the most common type of pancreatic cancer. Intratumor genomic heterogeneity within PDAC tumors has been reported by several studies (*4–7*), suggesting the genomic instability of PDAC cells. Moreover, two subtypes of PDAC cells were revealed by multiple transcriptomic studies (*8–11*): the more common classical/progenitor subtype and the more aggressive basal-like/squamous subtype. Interestingly, several recent studies have shown the existence of these subtypes within a PDAC tumor (*12–15*), suggesting the plasticity of PDAC cells and the phenotypic heterogeneity within the tumor, which might be driven by the genomic events during tumor evolution (*12, 13*). However, the underlying mechanisms behind PDAC genomic instability and the observed phenotypic and genomic heterogeneity are largely unknown. One possible approach to uncovering the underlying mechanisms of PDAC heterogeneity is to perform a mechanistic study using PDAC cell lines that show phenotypic and genomic heterogeneity.

MIA PaCa-2 is one of the commonly used primary tumor-derived PDAC cell lines (*16*). Genomically, MIA PaCa-2 has mutations within the three most frequently mutated genes in PDAC (*17*): G12C in *KRAS*, R248W in *TP53*, and homozygous deletion of *CDKN2A*. In addition, transcriptionally, MIA PaCa-2 cells have been categorized as the basal-like/squamous subtype (*8*). By isolating single-cell clones, several studies have shown that MIA PaCa-2 comprises cells with differential phenotypes in multiple aspects, including adhesion, integrin expression, anchorage-independent growth, and invasion (*18, 19*), suggesting the phenotypic heterogeneity of MIA PaCa-2 cells. Based on these findings, MIA PaCa-2 may be a good candidate on which to

perform a mechanistic study of PDAC heterogeneity. In this study, to evaluate its suitability for a mechanistic study, we aimed to further characterize the nature of MIA PaCa-2 phenotypic, genomic, and transcriptomic heterogeneity. First, we established MIA PaCa-2 clones through single-cell flow cytometry and chose four clones that display clear phenotypic differences in their cellular morphology, proliferation rate, and migration potential. Then, using a single-nucleotide polymorphism microarray (SNPa), we observed genomic heterogeneity between the MIA PaCa-2 clones in the form of chromosome copy number alterations. Our RNA-seq analysis also showed significant differences between the transcriptomic profiles of the clones. Lastly, from the transcriptomic analysis, we identified a gene, *Integrin Subunit Alpha V* (*ITGAV*), that is uniquely regulated between the clones and its modulation dictates MIA PaCa-2 cell morphology, suggesting a possible driver of the observed differences in cellular morphology, linking the phenotypic and transcriptional heterogeneity.

Results

Morphological heterogeneity of MIA PaCa-2 clones

To study whether heterogeneity exists in MIA PaCa-2 cells, we first flow-sorted a single cell into each well of a 96-well plate by forward scatter flow cytometry. Twenty-one single-cell clones were successfully established (**Figure S1**), from which we chose four for this study because they showed clear morphology differences (clones #1, #2, #3, and #4). Both clone #1 and clone #2 cells had a spindle-like morphology; however, clone #1 cells appeared to have a lower degree of cell spreading, resulting in a more elongated morphology. Clone #3 cells were cuboidal, whereas clone #4 cells were rounded and looked much smaller than cells from the other three clones (**Figure 1A**). We then quantified the cellular morphology of these four clones through three cell morphometric parameters (cell area, circularity, and aspect ratio in **Figure 1B**). Indeed, the cell surface area and the aspect ratio of clone #4 were significantly lower than the other three clones, whereas its circularity was significantly higher, reinforcing our observation of the rounded

morphology of the clone #4 population. Likewise, the aspect ratio of clone #1 was higher than clone #2, confirming the more elongated morphology of clone #1 cells. These results demonstrate morphological heterogeneity within MIA PaCa-2 cells.

Proliferation rate, migration potential, and gemcitabine sensitivity of MIA PaCa-2 clones

We then investigated whether the MIA PaCa-2 clones show other phenotypic differences, such as proliferation rate and migration potential. First, we seeded the same number of cells from the four MIA PaCa-2 clones at day 0, cultured them for 4 days, and imaged them every day from day 1 to day 4. Cell numbers were counted each day for each of the clones. We found that clone #1 was the fastest-proliferating cell line, while clone #3 was the slowest (**Figure 2A–B**). When compared with clone #4, the other three clones displayed significant differences on day 4. The result suggests a differential proliferation rate between the MIA PaCa-2 clones.

To investigate whether the MIA PaCa-2 clones have distinct migration rates, we utilized the scratch wound healing assay (*20, 21*). Since cell proliferation contributes to wound closure in the scratch wound healing assay, to only study cell migration in this assay, we blocked cell proliferation during the process of the assay by administration of DNA synthesis inhibitor thymidine (*22, 23*) in the cell culture medium 24 hours before introducing the scratch. Results indicated that wound closure was significantly faster in clone #1 and clone #2 after 48-hour culture relative to clone #3 and clone #4 (**Figure 2C,D**), suggesting the differential migration potential between the clones.

Gemcitabine is one of the first-line chemotherapeutic drugs for PDAC; it is an analog of deoxycytidine, which prevents cell growth through the inhibition of DNA synthesis (*24, 25*). To assess the cytotoxic effect of gemcitabine on the MIA PaCa-2 clones, we treated the four clones with a series of gemcitabine concentrations for 3 days, followed by a luminescence cell viability assay and calculation of half maximal inhibitory concentrations (IC_{50}), as a reflection of drug sensitivity. The IC_{50} was the lowest for clone #4 at 2.9 nM, followed by clones #3, #1, and #2 at

4.3 nM, 8.0 nM, and 10.1 nM, respectively (**Figure S2**). However, these differences are not statistically significant.

Genomic and transcriptomic heterogeneity between the MIA PaCa-2 clones

To investigate the level of genomic heterogeneity within the MIA PaCa-2 cells, we analyzed the chromosome copy number profiles of the clones using SNPa. We have previously shown that SNPa produced similar copy number profiles as the comparative genome hybridization array (*26*), which is the gold standard for chromosome copy number profile quantification (*27*). The genomic DNA of the MIA PaCa-2 clones was subjected to SNPa and the data was used to derive the copy number profiles at 1 Mb resolution (**Figure 3A**). Chromosome copy number alterations were observed across the genome of the MIA PaCa-2 clones, with distinct differences between the clones. To better visualize the copy number differences between the clones, we then derived the copy number variations (CNVs) between the MIA PaCa-2 clones (**Figure 3B**). CNVs that are unique to a clone were observed in chromosomes 1, 2, 3, 5, 7, 10, 11, 12, 14, 16, 22, and X. Results from SNPa and CNVs analysis suggest genomic heterogeneity within the MIA PaCa-2 population.

Next, to investigate the heterogeneity at the mRNA level, the MIA PaCa-2 clones were subjected to RNA-seq analysis. The normalized read counts of each clone were divided by the median count of each gene across the clones. This enabled us to observe the level of regulation of each gene across the clones. The genes that were uniquely regulated within a clone, with a fold change greater than the threshold ($-1 < \log2(FC) < 1$), were chosen and their level of regulation was visualized in a heatmap (**Figure 4**). Hierarchical clustering of the genes revealed eight clusters of genes that were uniquely regulated within a given clone. Clusters 1, 2, 4, and 6 were comprised of genes that were uniquely upregulated in clones #3, #4, #2, and #1, respectively. Meanwhile, clusters 3, 5, 7, and 8 contained genes that were uniquely

downregulated in clones #1, #4, #2, and #3, respectively. The RNA-seq analysis suggests a degree of transcriptomic heterogeneity within the MIA PaCa-2 population.

ITGAV dictates the morphology of MIA PaCa-2 clones

In typical cell culture, the extracellular matrix (ECM) proteins within the serum are adsorbed by the culture surface and cellular adhesion is initiated by the recognition of these proteins by integrins, followed by focal adhesion complex formation and maturation. Integrins are heterodimeric proteins found across the plasma membrane that connect the cells with the ECM by binding to specific recognition sites within ECM ligands (*28, 29*). Considering the importance of integrins in dictating cellular spreading and morphology, we were prompted to investigate whether any of the integrin genes are uniquely regulated between the clones, which may explain the morphological heterogeneity that we observed in Figure 1. Interestingly, *ITGAV* is listed in cluster 5 (**Figure 4**), which contains genes that are uniquely downregulated in clone #4, the clone with the rounded morphology. Indeed, the mRNA level of *ITGAV* was the lowest for clone #4 (**Figure 5A**) and this was also confirmed at the protein level through immunoblotting against ITGAV (**Figure 5B**). *ITGAV* encodes for the protein integrin αV, which can bind to the RGD motif of fibronectin and vitronectin as heterodimers αVβ1, αVβ3, αVβ5, αVβ6, and αVβ8 (*28, 29*). This depletion of *ITGAV* may be the cause of the rounded morphology of clone #4 cells.

To check whether ITGAV is sufficient to induce morphological changes in the MIA PaCa-2 clones, we first transiently expressed ITGAV proteins fused with the fluorescent protein mApple in the rounded clone #4. The overexpression of mApple-ITGAV induced morphological changes in the clone #4 cells, from rounded to a more elongated morphology (**Figure 5C–D**). Further quantification of the cellular morphology confirmed the significant differences between clone #4 cells with and without the expression of mApple-ITGAV (**Figure 5E**), suggesting that ITGAV can drive the spreading of clone #4 cells. Next, we used the CRISPR/Cas9 system to deplete the *ITGAV* expression in clone #1 (**Figure 5F**). We chose clone #1 cells because of their elongated

morphology. Indeed, knockout of *ITGAV* caused rounding of clone #1 cells (**Figure 5G, H**). Quantification of the cell morphology parameters confirmed the significant morphological changes of clone #1 upon loss of *ITGAV* (**Figure 5I**). Taken together, these results suggested that *ITGAV* expression level can dictate the cellular morphology of MIA PaCa-2 cells.

Discussion

The findings in this study showed that MIA PaCa-2 is comprised of cells with distinctive phenotypes, heterogeneous genomes, and differential transcriptomic profiles, suggesting its suitability as a model to study the underlying mechanisms behind PDAC tumor phenotypic and genomic heterogeneity. We can start such study with a single-cell clonal population, followed by subsequent cloning and genomic analysis to obtain the intrinsic genomic instability level of the cells. We can then investigate the role of the known PDAC driver genes on genomic variations by genetically modulating the corresponding genes and monitoring for any deviation from the intrinsic genomic instability level.

Of note, in this study we did not characterize the epigenomic heterogeneity of the MIA PaCa-2 cells. Epigenomic heterogeneity in PDAC tumors has been reported by several studies and it was associated with tumor aggressiveness and patient prognosis (*30, 31*), suggesting the critical role of the epigenetic landscape in PDAC progression. Further characterization of the MIA PaCa-2 epigenome is needed to check whether MIA PaCa-2 is a suitable model for studying the mechanisms that regulate PDAC epigenomic heterogeneity and its downstream impact on the heterogeneous transcriptomic profiles. Cancer cell lines are versatile models for studying cancer biology, enabling researchers to perform in-depth mechanistic studies at a fraction of the cost, time, and labor required by animal or human studies. However, the use of cell lines comes with various limitations, one of them being the phenotypic and genomic shift associated with decades of culture on plastic surfaces, compromising the cell line's relevance to the original tumor (*32*). One alternative to this issue is the use of PDAC organoids derived from patient tumors (*33–39*).

These organoids provide researchers with the opportunity to perform various *in vitro* mechanistic studies on a model that closely recapitulates the *in vivo* tumor phenotype, genotype, and even drug response. Furthermore, several studies have shown genomic and transcriptomic heterogeneity within PDAC organoids (*15, 40*), suggesting that organoids are suitable for studying genomic instability in PDAC.

Materials and Methods

Cell culture

The MIA PaCa-2 human pancreatic cell line was obtained from ATCC. Cells were maintained in Dulbecco's modified Eagles medium (DMEM) supplemented with 10% fetal bovine serum (Genesee Scientific) and 1% penicillin-streptomycin (Sigma-Aldrich). MIA PaCa-2 clones were generated by single-cell flow cytometry sorting at Florida State University's Flow Cytometry Laboratory. Briefly, MIA PaCa-2 cells were harvested after dissociation with trypsin (Corning) at 37°C for 5 minutes. Cells were washed once with PBS and resuspended with 1 ml of PBS supplemented with 10% fetal bovine serum and 1% penicillin-streptomycin. Cell suspensions were filtered through a BD FACS tube with a 70 µm strainer top. Single cells were sorted using the FACSCanto instrument (BD) by forward scatter to a 96-well plate (Genesee Scientific). Twenty-one MIA PaCa-2 single-cell clones were established after approximately 3 weeks of culture, and four of the 21 clones were expanded and used in this study. *ITGAV* overexpression was achieved by 24-hour transfection with Lipofectamine 2000 (ThermoFisher); the mApple-Alpha-V-Integrin-25 was a gift from Michael Davidson (Addgene plasmid # 54866; http://n2t.net/addgene:54866; RRID: Addgene_54866). For *ITGAV* depletion, three gRNAs were selected by using CRISPick (*41, 42*) and cloned into lentiCRISPR v2 plasmid (*43*), a gift from Feng Zhang (Addgene plasmid # 52961; http://n2t.net/addgene:52961; RRID: Addgene_52961). Lentiviral particles were produced through the transfection of the transfer plasmid, lentiCRISPR v2, and the packaging plasmids, psPAX2 (a gift from Didier Trono, Addgene plasmid # 12260;

http://n2t.net/addgene:12260; RRID: Addgene_12260) and pCMV-VSV-G (*44*) (a gift from Bob Weinberg, Addgene plasmid # 8454; http://n2t.net/addgene:8454; RRID: Addgene_8454), into the HEK293T cells by using the TransIT-Lenti transfection reagent (Mirus Bio). Lentiviral transduction of the CRISPR construct was performed with 10 µg/mL polybrene (ThermoFisher).

Scratch wound healing assay

Cell migration was evaluated by a scratch wound healing assay as previously described (*20, 21*). MIA PaCa-2 clone cells were seeded at a concentration of 100,000 cells/cm^2 (80% confluent) in 12-well plates and cultured under normal culture medium until reaching fully confluent. 2 mM thymidine was introduced to the cells to block cell proliferation for 24 hours. Next, each well was artificially wounded in the middle by creating a scratch with a 1000 µL tip plastic pipette on the cell monolayer. Each well was washed once with PBS to remove the floating cells and then cultured under a normal culture medium supplemented with 2 mM thymidine until the end of the assay. Images of scratch wounds were captured using an EVOS microscope (ThermoFisher) at 0, 24, and 48 hours after the scratch. The wound closure areas were measured with ImageJ (*45*) after 24 and 48 hours. To avoid scratch area variation, the relative wound closure area was calculated as [%] = (wound closure area^{T0} - wound closure area^{T48}) * 100 [%]/wound closure area^{T0}.

Western blot

Western blotting was performed using standard methods. Briefly, cell pellets were harvested and resuspended in RIPA buffer with the addition of a phosphatase inhibitor cocktail as 50 µL buffer per million cells. Cell suspensions were then sonicated for 15 seconds and immediately put on ice for 30 minutes and cleared by centrifugation for 30 minutes at maximum speed. 10–15 µL of protein lysis were run per lane of 4–12% Bis-Tris gels (Thermo Fisher Scientific) using MOPS buffer. Proteins were transferred to nitrocellulose membrane at 20 V for 7 minutes using the

iBlot™ 2 Transfer Stack (Thermo Fisher Scientific). Membranes were blocked in 5% non-fat milk powder in TBS+0.1% Tween (TBST) and incubated overnight at 4°C in primary antibody diluted in TBS solution at 1 μg/mL. Primary antibodies used were rabbit monoclonal antibody against ITGAV (ab179475, Abcam) and mouse monoclonal antibody against β-Actin (sc-47778, Santa Cruz Biotechnology). Membranes were incubated with corresponding horseradish peroxidase-conjugated second antibodies at room temperature for 1 hour. After three washes in TBST, membranes were exposed to ChromoSensor™ One-Solution (GenScript) for 3–5 minutes. Membranes were quickly washed three times with water and imaged.

Single nucleotide polymorphism microarray

DNA isolation was performed using the Blood and Cell Culture DNA Mini Kit (QIAGEN). The isolated DNA samples were sent to the Center for Applied Genomics at the Children's Hospital of Philadelphia for the SNP array analysis using the Infinium Global Screening Array-24 v3.0 Kit (Illumina). The chromosome copy number analysis was performed in GenomeStudio v.2.0 (Illumina) by using the cnvPartition v.3.2.1 plugin. The chromosome copy number calls were averaged every 1 Mb to derive the copy number profiles at 1 Mb resolution. Heatmaps were plotted in R by using the algorithm gtrellis v.1.28.0 (*46*).

RNA-seq sample preparation and analysis

RNA isolation from the MIA PaCa-2 clones was performed by using the RNeasy Plus Micro Kit (QIAGEN). Libraries for RNA-seq were made with the NEBNext Ultra II Directional RNA Library Prep Kit for Illumina (NEB) per the manufacturer's instructions, followed by 150-bp paired-end sequencing with the Novaseq 6000 at Florida State University's Translational Science Laboratory, resulting in ~25,000,000 reads for each sample. Reads per kilobase million for each gene were calculated by normalization of the read of each gene by the sample's total read count (in millions)

and by the gene length (in kilobases). The gene expression profile was plotted in R by using the algorithm gtrellis v.1.28.0 (*46*).

Acknowledgment

The authors would like to thank Drs. Cynthia Vied and Yanming Yang at Florida State University's Translational Science Laboratory for running the RNA-seq libraries and Dr. Beth Alexander at Florida State University's Flow Cytometry Laboratory for helping isolate the MIA PaCa-2 clones. We are grateful for the great service from the team at Florida State University's Biology Core Facilities. The authors would like to thank Dr. Terra Bradley for the careful editing of the manuscript. The authors thank all the lab members in Dr. Jerome Irianto's and Dr. Yue Julia Wang's laboratories for their valuable suggestions and assistance. The authors in this study were supported by startup funds from Florida State University, awards from the Florida Department of Health's Bankhead-Coley Cancer Research Program (award number 21B11) and Live Like Bella Pediatric Cancer Research Initiative (award number 23L06), and a collaborative Trans-Network Project linked to the Physical Science-Oncology Project 5U01 CA214282 from the National Cancer Institute of the National Institutes of Health.

References

1. P. C. Nowell, The clonal evolution of tumor cell populations. *Science* **194**, 23-28 (1976).
2. M. Greaves, C. C. Maley, Clonal evolution in cancer. *Nature* **481**, 306-313 (2012).
3. A. Marusyk, M. Janiszewska, K. Polyak, Intratumor Heterogeneity: The Rosetta Stone of Therapy Resistance. *Cancer Cell* **37**, 471-484 (2020).
4. S. Yachida *et al.*, Distant metastasis occurs late during the genetic evolution of pancreatic cancer. *Nature* **467**, 1114-1117 (2010).
5. P. J. Campbell *et al.*, The patterns and dynamics of genomic instability in metastatic pancreatic cancer. *Nature* **467**, 1109-1113 (2010).

6. A. P. Makohon-Moore *et al.*, Limited heterogeneity of known driver gene mutations among the metastases of individual patients with pancreatic cancer. *Nat Genet* **49**, 358-366 (2017).

7. S. C. Dentro *et al.*, Characterizing genetic intra-tumor heterogeneity across 2,658 human cancer genomes. *Cell* **184**, 2239-2254 e2239 (2021).

8. R. A. Moffitt *et al.*, Virtual microdissection identifies distinct tumor- and stroma-specific subtypes of pancreatic ductal adenocarcinoma. *Nat Genet* **47**, 1168-1178 (2015).

9. E. A. Collisson *et al.*, Subtypes of pancreatic ductal adenocarcinoma and their differing responses to therapy. *Nat Med* **17**, 500-503 (2011).

10. P. Bailey *et al.*, Genomic analyses identify molecular subtypes of pancreatic cancer. *Nature* **531**, 47-52 (2016).

11. a. a. d. h. e. Cancer Genome Atlas Research Network. Electronic address, N. Cancer Genome Atlas Research, Integrated Genomic Characterization of Pancreatic Ductal Adenocarcinoma. *Cancer Cell* **32**, 185-203 e113 (2017).

12. M. Chan-Seng-Yue *et al.*, Author Correction: Transcription phenotypes of pancreatic cancer are driven by genomic events during tumor evolution. *Nat Genet* **52**, 463 (2020).

13. A. Hayashi *et al.*, A unifying paradigm for transcriptional heterogeneity and squamous features in pancreatic ductal adenocarcinoma. *Nat Cancer* **1**, 59-74 (2020).

14. N. Juiz *et al.*, Basal-like and classical cells coexist in pancreatic cancer revealed by single-cell analysis on biopsy-derived pancreatic cancer organoids from the classical subtype. *FASEB J* **34**, 12214-12228 (2020).

15. T. G. Krieger *et al.*, Single-cell analysis of patient-derived PDAC organoids reveals cell state heterogeneity and a conserved developmental hierarchy. *Nat Commun* **12**, 5826 (2021).

16. M. Wu, G. K. Arimura, A. A. Yunis, Purification and characterization of a plasminogen activator secreted by cultured human pancreatic carcinoma cells. *Biochemistry* **16**, 1908-1913 (1977).

17. E. L. Deer *et al.*, Phenotype and genotype of pancreatic cancer cell lines. *Pancreas* **39**, 425-435 (2010).

18. N. Walsh, M. Clynes, J. Crown, N. O'Donovan, Alterations in integrin expression modulates invasion of pancreatic cancer cells. *J Exp Clin Cancer Res* **28**, 140 (2009).

19. N. Walsh *et al.*, Identification of pancreatic cancer invasion-related proteins by proteomic analysis. *Proteome Sci* **7**, 3 (2009).

20. L. G. Rodriguez, J. L. Guan, 14-3-3 regulation of cell spreading and migration requires a functional amphipathic groove. *J Cell Physiol* **202**, 285-294 (2005).

21. A. Grada, M. Otero-Vinas, F. Prieto-Castrillo, Z. Obagi, V. Falanga, Research Techniques Made Simple: Analysis of Collective Cell Migration Using the Wound Healing Assay. *J Invest Dermatol* **137**, e11-e16 (2017).

22. G. Chen, X. Deng, Cell Synchronization by Double Thymidine Block. *Bio Protoc* **8**, (2018).

23. J. B. Schvartzman, D. B. Krimer, J. Van't Hof, The effects of different thymidine concentrations on DNA replication in pea-root cells synchronized by a protracted 5-fluorodeoxyuridine treatment. *Exp Cell Res* **150**, 379-389 (1984).

24. J. Yang *et al.*, Ferroptosis: At the Crossroad of Gemcitabine Resistance and Tumorigenesis in Pancreatic Cancer. *Int J Mol Sci* **22**, (2021).

25. S. Dent, H. Messersmith, M. Trudeau, Gemcitabine in the management of metastatic breast cancer: a systematic review. *Breast Cancer Res Treat* **108**, 319-331 (2008).

26. J. Irianto *et al.*, DNA Damage Follows Repair Factor Depletion and Portends Genome Variation in Cancer Cells after Pore Migration. *Curr Biol* **27**, 210-223 (2017).

27. N. P. Carter, Methods and strategies for analyzing copy number variation using DNA microarrays. *Nat Genet* **39**, S16-21 (2007).

28. R. O. Hynes, Integrins: bidirectional, allosteric signaling machines. *Cell* **110**, 673-687 (2002).

29. J. D. Humphries, A. Byron, M. J. Humphries, Integrin ligands at a glance. *J Cell Sci* **119**, 3901-3903 (2006).

30. X. Fan *et al.*, Integrated single-cell multiomics analysis reveals novel candidate markers for prognosis in human pancreatic ductal adenocarcinoma. *Cell Discov* **8**, 13 (2022).

31. G. Lomberk *et al.*, Distinct epigenetic landscapes underlie the pathobiology of pancreatic cancer subtypes. *Nat Commun* **9**, 1978 (2018).

32. S. Domcke, R. Sinha, D. A. Levine, C. Sander, N. Schultz, Evaluating cell lines as tumour models by comparison of genomic profiles. *Nat Commun* **4**, 2126 (2013).

33. M. Huch *et al.*, Unlimited in vitro expansion of adult bi-potent pancreas progenitors through the Lgr5/R-spondin axis. *EMBO J* **32**, 2708-2721 (2013).

34. S. F. Boj *et al.*, Organoid models of human and mouse ductal pancreatic cancer. *Cell* **160**, 324-338 (2015).

35. H. Tiriac *et al.*, Organoid Profiling Identifies Common Responders to Chemotherapy in Pancreatic Cancer. *Cancer Discov* **8**, 1112-1129 (2018).

36. E. Driehuis *et al.*, Pancreatic cancer organoids recapitulate disease and allow personalized drug screening. *Proc Natl Acad Sci U S A*, (2019).

37. L. Huang *et al.*, Ductal pancreatic cancer modeling and drug screening using human pluripotent stem cell- and patient-derived tumor organoids. *Nat Med* **21**, 1364-1371 (2015).

38. A. J. Walsh, J. A. Castellanos, N. S. Nagathihalli, N. B. Merchant, M. C. Skala, Optical Imaging of Drug-Induced Metabolism Changes in Murine and Human Pancreatic Cancer Organoids Reveals Heterogeneous Drug Response. *Pancreas* **45**, 863-869 (2016).

39. T. Seino *et al.*, Human Pancreatic Tumor Organoids Reveal Loss of Stem Cell Niche Factor Dependence during Disease Progression. *Cell Stem Cell* **22**, 454-467 e456 (2018).

40. O. H. Usman *et al.*, Genomic heterogeneity in pancreatic cancer organoids and its stability with culture. *NPJ Genom Med* **7**, 71 (2022).

41. K. R. Sanson *et al.*, Optimized libraries for CRISPR-Cas9 genetic screens with multiple modalities. *Nat Commun* **9**, 5416 (2018).

42. J. G. Doench *et al.*, Optimized sgRNA design to maximize activity and minimize off-target effects of CRISPR-Cas9. *Nat Biotechnol* **34**, 184-191 (2016).

43. N. E. Sanjana, O. Shalem, F. Zhang, Improved vectors and genome-wide libraries for CRISPR screening. *Nat Methods* **11**, 783-784 (2014).

44. S. A. Stewart *et al.*, Lentivirus-delivered stable gene silencing by RNAi in primary cells. *RNA* **9**, 493-501 (2003).

45. C. A. Schneider, W. S. Rasband, K. W. Eliceiri, NIH Image to ImageJ: 25 years of image analysis. *Nat Methods* **9**, 671-675 (2012).

46. Z. Gu, R. Eils, M. Schlesner, gtrellis: an R/Bioconductor package for making genome-level Trellis graphics. *BMC Bioinformatics* **17**, 169 (2016).

Figure 1

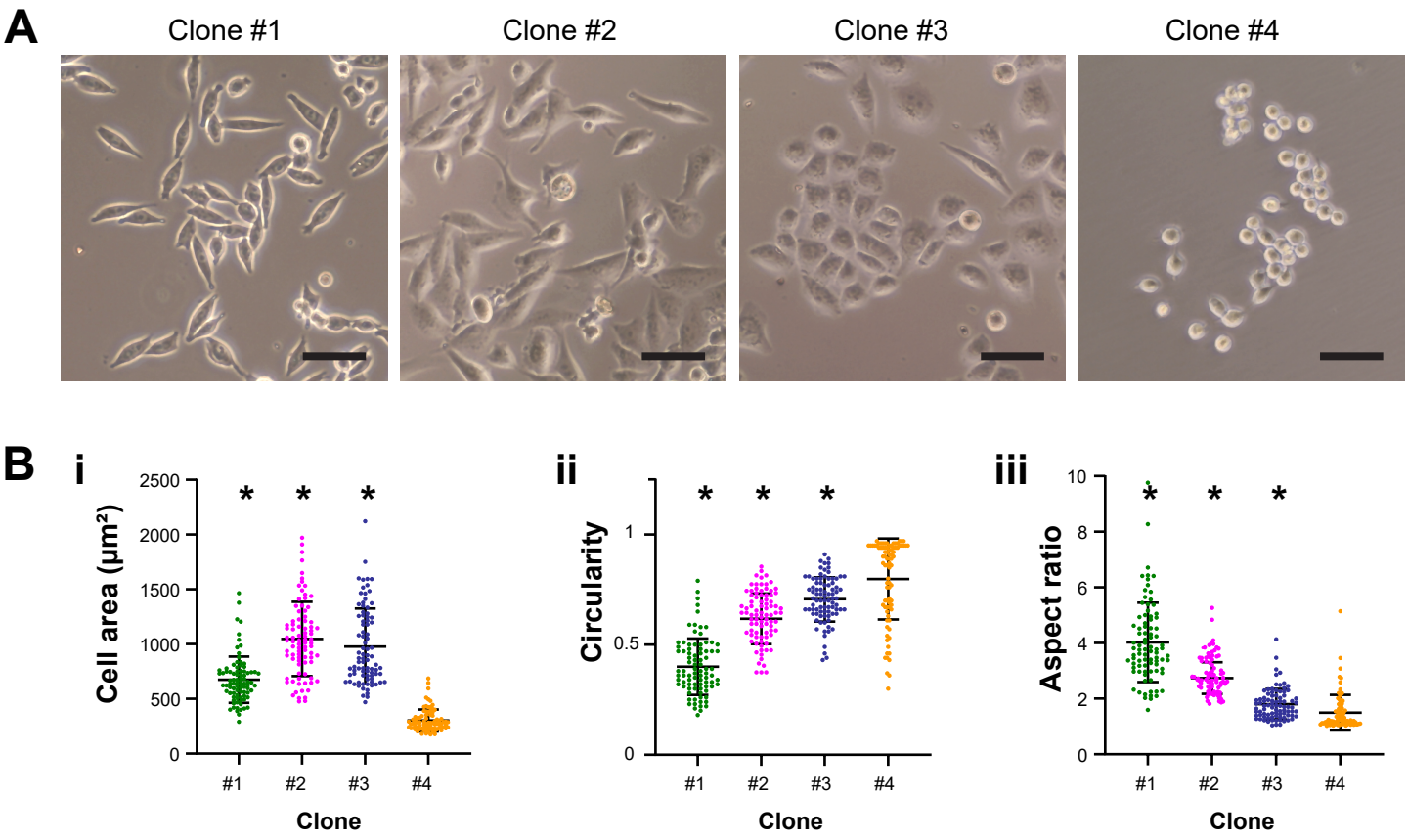
A
Clone #1
Clone #2
Clone #3
Clone #4
B
i
Cell area (μm²)
2500
2000
1500
1000
500
0
*
*
*
#1
#2
#3
#4
Clone
ii
Circularity
1
0.5
0
*
*
*
#1
#2
#3
#4
Clone
iii
Aspect ratio
10
8
6
4
2
0
*
*
*
#1
#2
#3
#4
Clone

Figure 1. Morphological heterogeneity of MiaPaCa-2 clones. (**A**) Representative images of four MiaPaCa-2 clones isolated and expanded from single-cell flow sorting, showing their morphological differences (scale bar = 50 μm). (**B**) Three cell morphometric parameters (cell area, circularity, and aspect ratio) were analyzed by ImageJ, showing significant differences against the rounded clone #4 (N = 3 experiments, Welch's t-test, $p < 0.05$ vs. clone #4).

Figure 2

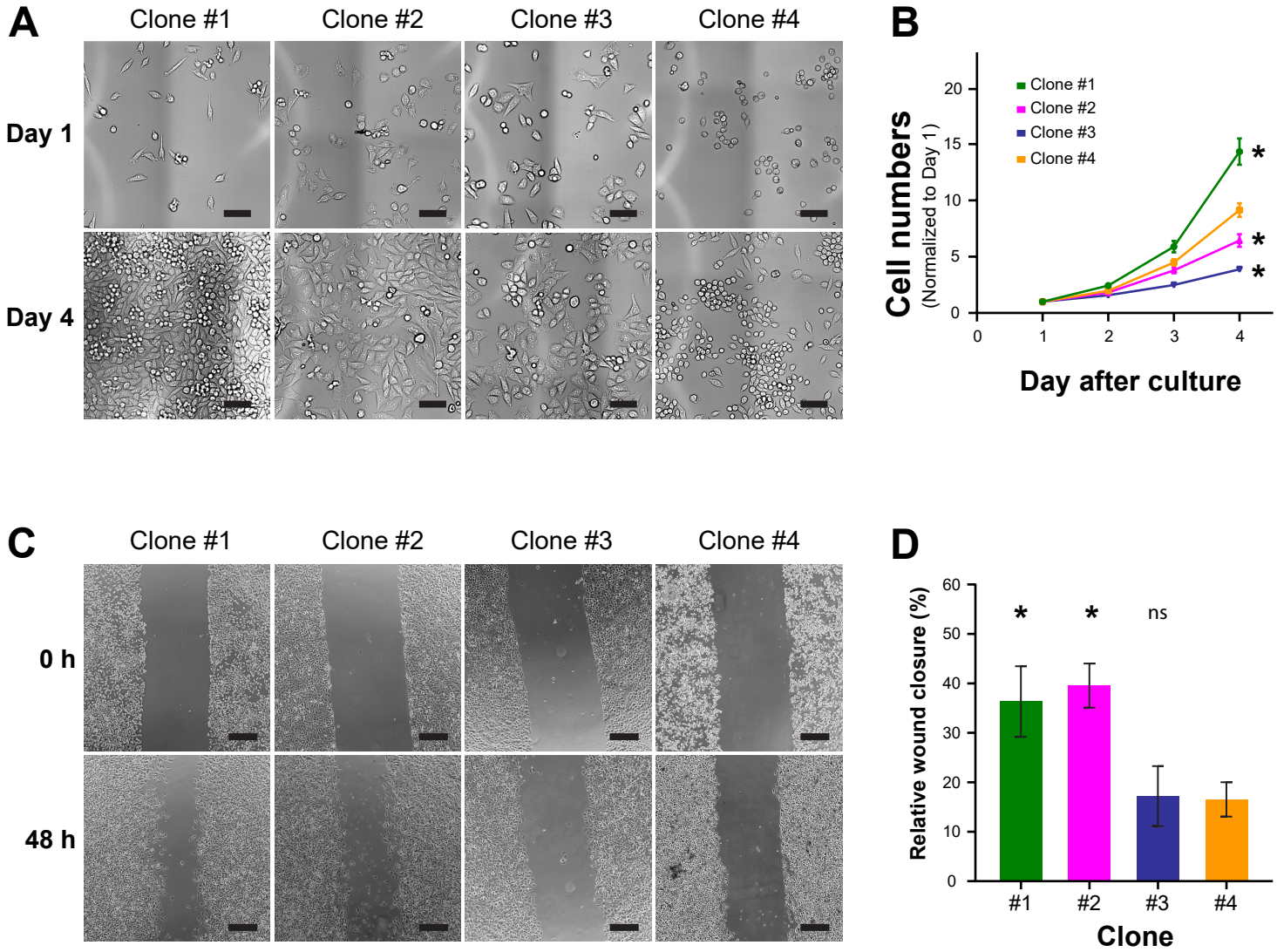
A
Clone #1
Clone #2
Clone #3
Clone #4
Day 1
Day 4
B
Clone #1
Clone #2
Clone #3
Clone #4
Cell numbers
(Normalized to Day 1)
Day after culture
C
Clone #1
Clone #2
Clone #3
Clone #4
0 h
48 h
D
Relative wound closure (%)
ns
#1
#2
#3
#4
Clone

Figure 2. Differential proliferation and migration rate of MiaPaCa-2 clones. (**A**) Representative images of the MiaPaCa-2 clone cells on day 1 and day 4 after seeding (scale bar = 100 μm). (**B**) The plot of cell numbers of different MiaPaCa-2 clones over a 4-day culture period. The cell numbers were normalized to the cell number of day 1 in each of the clones. (**C**) Representative images of the scratch wound healing assay of the four MiaPaCa-2 clones at zero and 48 hours after the scratch (scale bar = 300 μm). (**D**) The plot of the relative wound closure of the different MiaPaCa-2 clones at 48 hours (N = 3 experiments, Welch's t-test, $p < 0.05$ vs. clone #4).

Figure 3

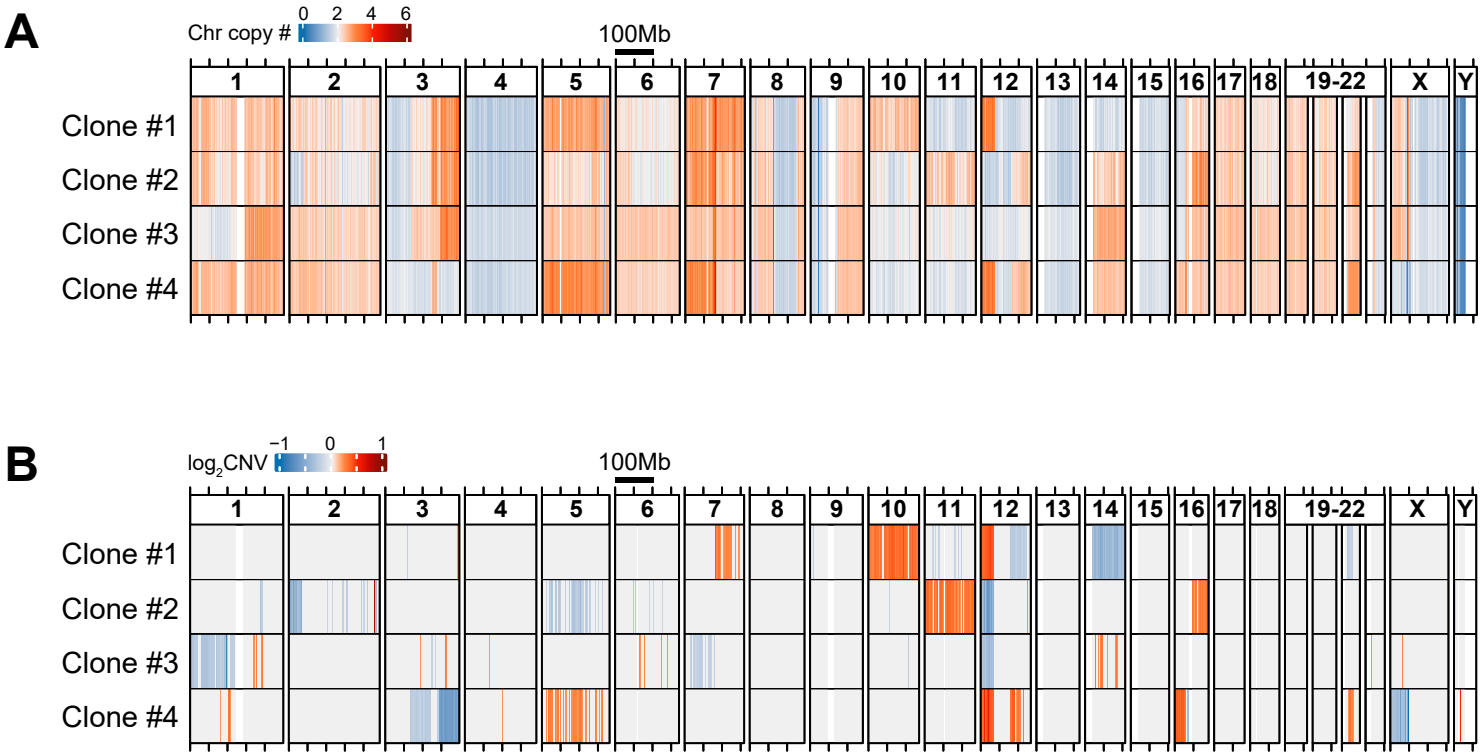
A
Chr copy #
0 2 4 6
100Mb
1 2 3 4 5 6 7 8 9 10 11 12 13 14 15 16 17 18 19-22 X Y
Clone #1
Clone #2
Clone #3
Clone #4
B
log2CNV
−1 0 1
100Mb
1 2 3 4 5 6 7 8 9 10 11 12 13 14 15 16 17 18 19-22 X Y
Clone #1
Clone #2
Clone #3
Clone #4

Figure 3. Genomic heterogeneity between the MiaPaCa-2 clones. (**A**) Genomic DNA of the MiaPaCa-2 clones was subjected to SNPa and the resulting data were used to derive chromosome copy numbers of the clones within 1 Mb binning windows. The heatmaps illustrate chromosome copy numbers across the whole genome, where blue indicates chromosome loss (<2) and red indicates chromosome gain (>2). (**B**) The copy number variations (CNVs) between the clones were derived by dividing the copy number of each clone by the median copy number. CNVs that are unique to a clone were observed in chromosomes 1, 2, 3, 5, 7, 10, 11, 12, 14, 16, 22, and X, suggesting genomic heterogeneity between the clones.

Figure 4

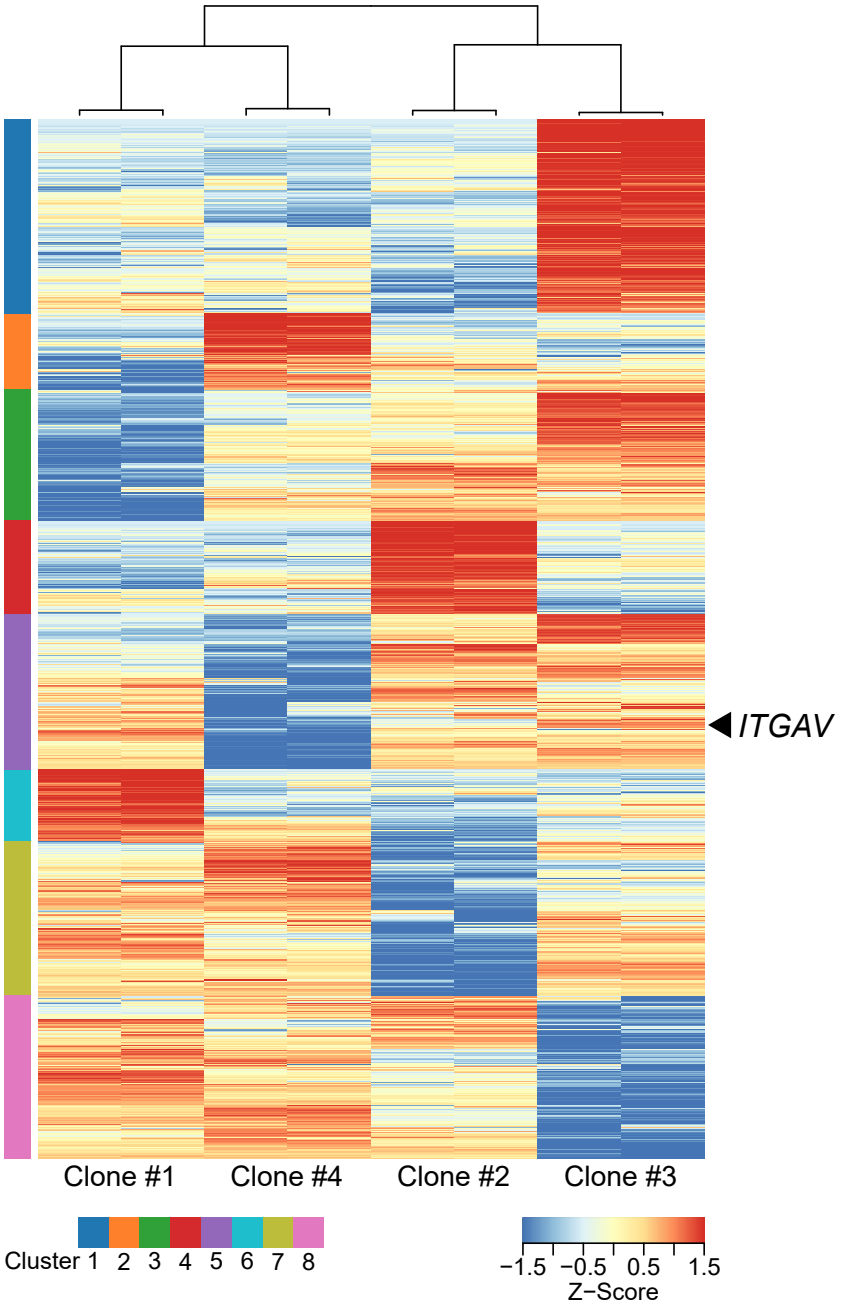
ITGAV
Clone #1
Clone #4
Clone #2
Clone #3
Cluster 1 2 3 4 5 6 7 8
−1.5 −0.5 0.5 1.5
Z−Score

Figure 4. Differential gene expressions between the MiaPaCa-2 clones. The MiaPaCa-2 clones were subjected to RNA-seq. The normalized read counts of each clone were divided by the median count of each gene to derive the differentially regulated genes between the clones. The heatmap contains the normalized read counts of genes that were uniquely regulated within a clone, with a threshold of $-1 < \log2(FC) < 1$. Hierarchical clustering of the genes revealed the group of genes that were uniquely regulated within a given clone.

Figure 5

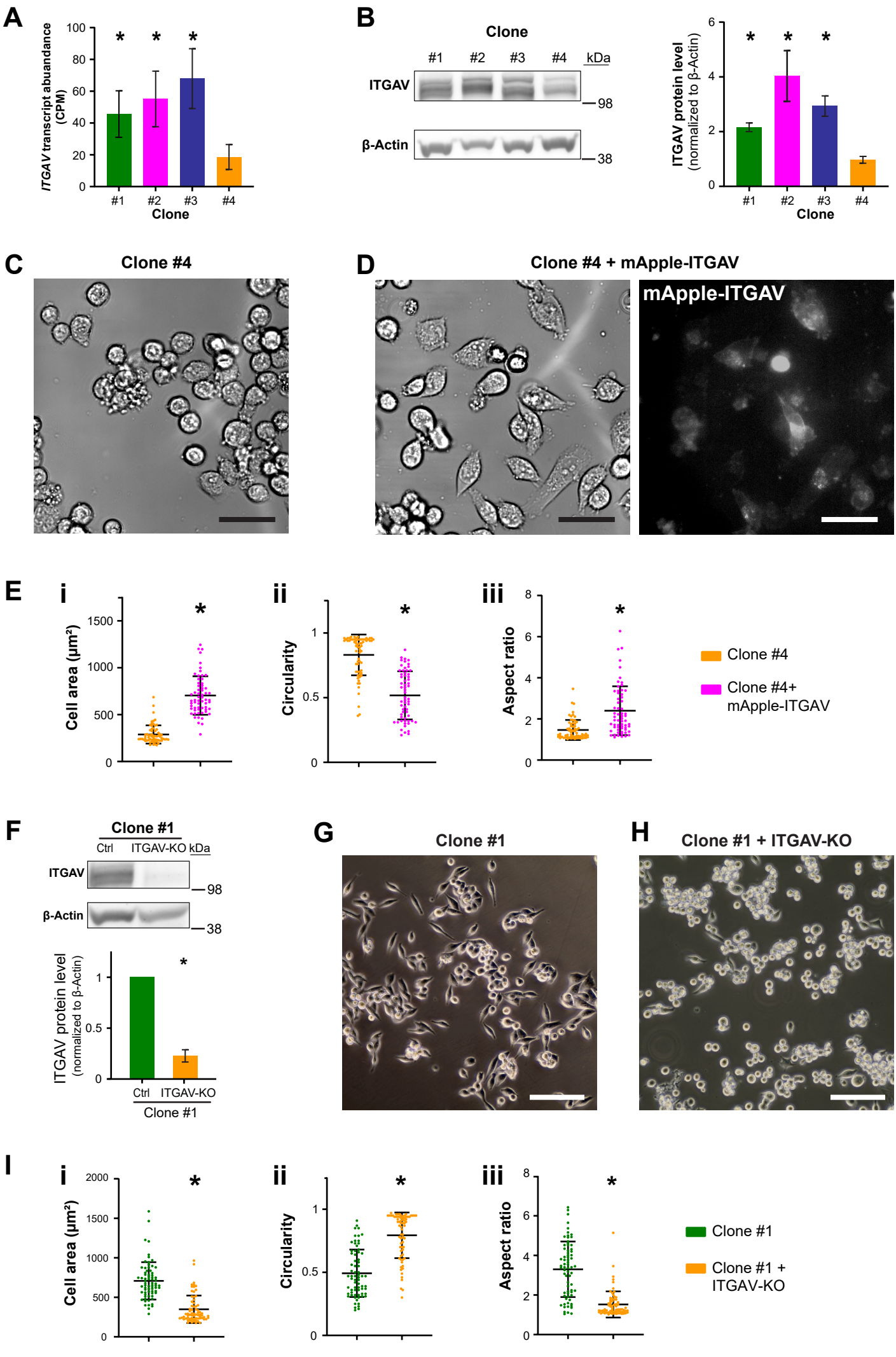
A
ITGAV transcript abuandance (CPM)
100
80
60
40
20
0
*
*
*
#1
#2
#3
#4
Clone
B
Clone
#1
#2
#3
#4
kDa
ITGAV
98
β-Actin
38
ITGAV protein level (normalized to β-Actin)
6
4
2
0
*
*
*
#1
#2
#3
#4
Clone
C
Clone #4
D
Clone #4 + mApple-ITGAV
mApple-ITGAV
E
i
Cell area (μm²)
1500
1000
500
0
*
ii
Circularity
1
0.5
0
*
iii
Aspect ratio
8
6
4
2
0
*
Clone #4
Clone #4+ mApple-ITGAV
F
Clone #1
Ctrl
ITGAV-KO
kDa
ITGAV
98
β-Actin
38
ITGAV protein level (normalized to β-Actin)
1
0.5
0
*
Ctrl
ITGAV-KO
Clone #1
G
Clone #1
H
Clone #1 + ITGAV-KO
I
i
Cell area (μm²)
2000
1500
1000
500
0
*
ii
Circularity
1
0.5
0
*
iii
Aspect ratio
8
6
4
2
0
*
Clone #1
Clone #1 + ITGAV-KO

Figure 5. *ITGAV* dictates the cellular morphology of MiaPaCa-2 clones. (**A**) *ITGAV* read counts from the RNA-seq of the MiaPaCa-2 clones (normalized to counts per million reads, CPM), showing clone #4 had significantly decreased expression of *ITGAV* (Welch's t-test, $p < 0.05$). (**B**) Western blot of the ITGAV protein in the MiaPaCa-2 clones (upper band) and the β-Actin protein as the loading control (lower band) (left). Quantification of the ITGAV protein level, normalized to β-Actin, showing clone #4 had a significantly lower level of the ITGAV protein (Welch's t-test, $p < 0.05$ vs. clone #4, right). (**C** and **D**) Representative images of the MiaPaCa-2 clone #4 and clone #4 transiently transfected with mApple-ITGAV, showing that clone #4 cells were elongated when transfected with ITGAV (mApple positive) (scale bar = 50 μm). (**E**) Three cell morphometric parameters (cell area, circularity, and aspect ratio) were analyzed by ImageJ, showing significant differences between clone #4 and clone #4 expressing mApple-ITGAV (Welch's t-test, $p < 0.05$ vs. clone #4). (**F**) Western blot showing clone #1 upon knockout of *ITGAV* significantly reduced the ITGAV protein level (normalized to β-Actin, Welch's t-test, $p < 0.05$ vs. Ctrl). (**G** and **H**) Representative images of the MiaPaCa-2 clone #1 and clone #1 transduced with a CRISPR vector targeting *ITGAV*, showing that the majority of clone #1 cells upon depletion of *ITGAV* changed from elongated to rounded morphology (scale bar = 100 μm). (**I**) Three cell morphometric parameters (cell area, circularity, and aspect ratio) were analyzed by ImageJ, showing significant differences between clone #1 and clone #1 with the depletion of *ITGAV* (Welch's t-test, $p < 0.05$ vs. clone #1).

Figure S1

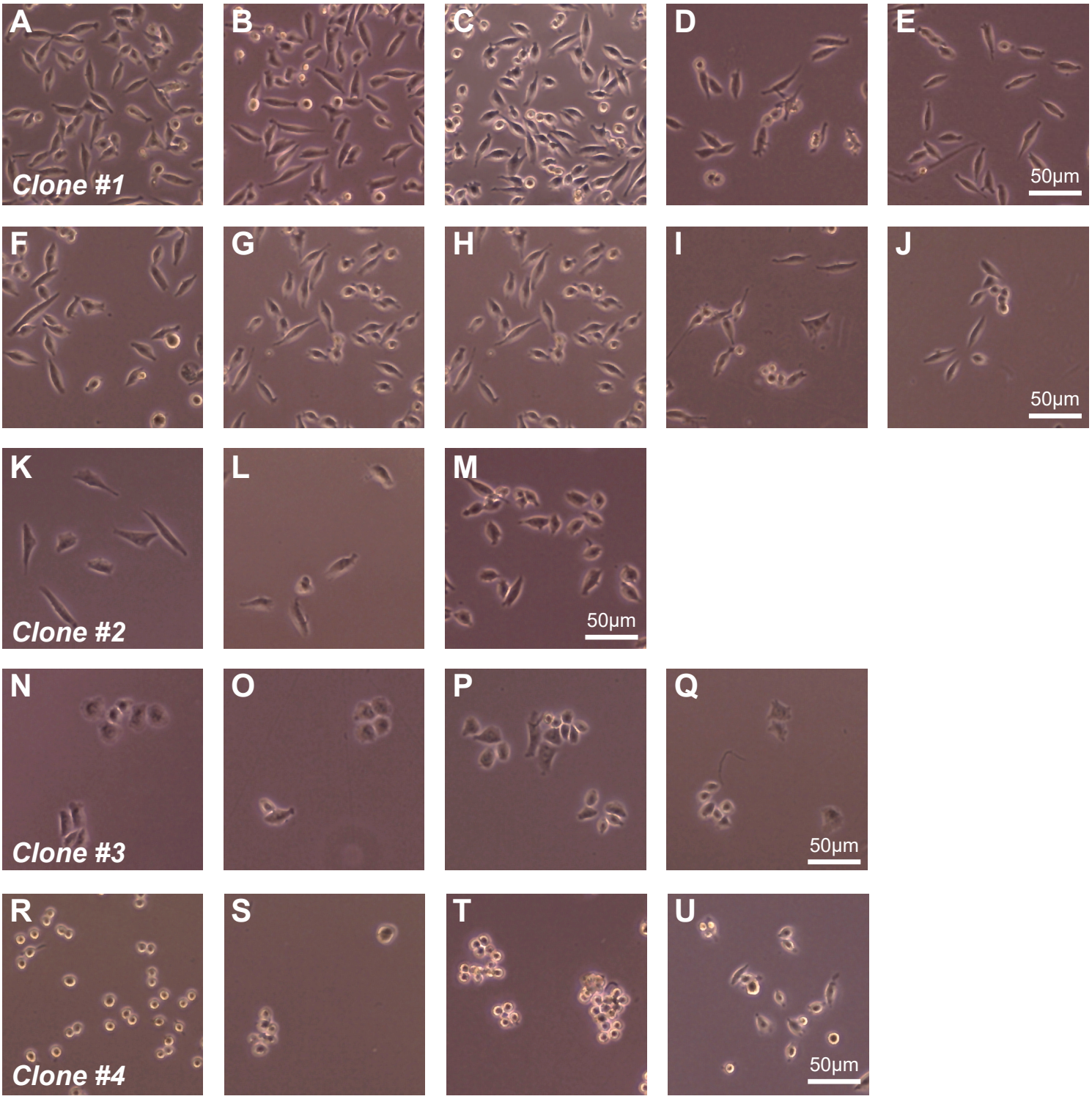
A
B
C
D
E
Clone #1
50µm
F
G
H
I
J
50µm
K
L
M
Clone #2
50µm
N
O
P
Q
Clone #3
50µm
R
S
T
U
Clone #4
50µm

Figure S1. Representative images of the 21 single-cell clones established from the MIA PaCa-2 bulk population, showing heterogeneous cellular morphology. A = Clone #1, K = Clone #2, N = Clone #3, and R = Clone #4.

Figure S2

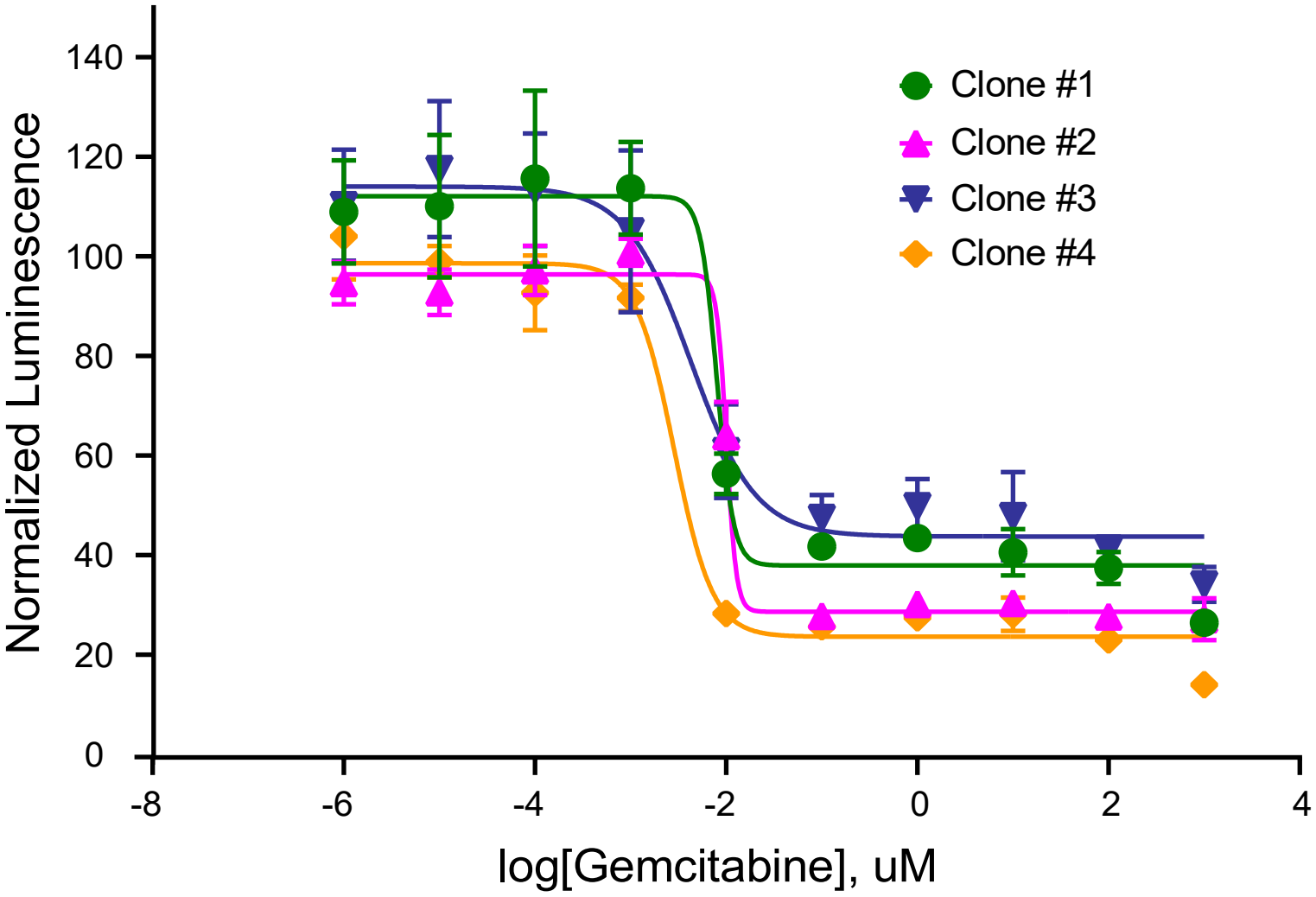
Normalized Luminescence
140
120
100
80
60
40
20
0
-8
-6
-4
-2
0
2
4
log[Gemcitabine], uM
Clone #1
Clone #2
Clone #3
Clone #4

Figure S2. MIA PaCa-2 clones #1, #2, #3, and #4 were treated with gemcitabine for 72 hours and the cell numbers were measured using a luminescence cell viability assay. The IC_{50} for clones #1, #2, #3, and #4 were 8 nM, 10.1 nM, 4.3 nM, and 2.9 nM respectively (N = 3 experiments, n = 2–3 wells).